ACS APPLIED MATERIALS & INTERFACES

www.acsami.org

Research Article

Broad Applicability of Electrochemical Impedance Spectroscopy to the Measurement of Oxygen Nonstoichiometry in Mixed Ion and Electron Conductors

Ruiyun Huang, Connor G. Carr, Chirranjeevi Balaji Gopal, and Sossina M. Haile*

Cite This: *ACS Appl. Mater. Interfaces* 2022, 14, 19629–19643

Read Online

ACCESS | Metrics & More | Article Recommendations | Supporting Information

ABSTRACT: Oxygen nonstoichiometry is a fundamental feature of mixed ion and electron conductors (MIECs). In this work, a general electrochemical method for determining nonstoichiometry in thin film MIECs, via measurement of the chemical capacitance, is demonstrated using ceria and ceria-zirconia ($Ce_{0.8}Zr_{0.2}O_{2-\delta}$) as representative materials. A.C. impedance data are collected from both materials at high temperature (750−900 °C) under reducing conditions with oxygen partial pressure (pO_2) in the range 10^{-13} to 10^{-20} atm. Additional measurements of ceria-zirconia films are made under relatively oxidizing conditions with pO_2 in the range 0.2 to 10^{-4} atm and temperatures of 800−900 °C. Under reducing conditions, the impedance spectra are described by a simple circuit in which a resistor is in series with a resistor and capacitor in parallel, and thickness-dependent measurements are used to resolve the capacitance into interfacial and chemical terms. Under more oxidizing conditions, the impedance spectra (of $Ce_{0.8}Zr_{0.2}O_{2-\delta}$) reveal an additional diffusional feature, which enables determination of the ionic resistance of the film in addition to the capacitance, and hence the transport properties. A generalized mathematical formalism is presented for recovering the nonstoichiometry from the chemical capacitance, without recourse to defect chemical models. The ceria nonstoichiometry values are in good agreement with literature values determined by thermogravimetric measurements but display considerably less scatter and are collected on considerably shorter time scales. The thermodynamic analysis of $Ce_{0.8}Zr_{0.2}O_{2-\delta}$ corroborates earlier findings that introduction of Zr into ceria enhances its reducibility.

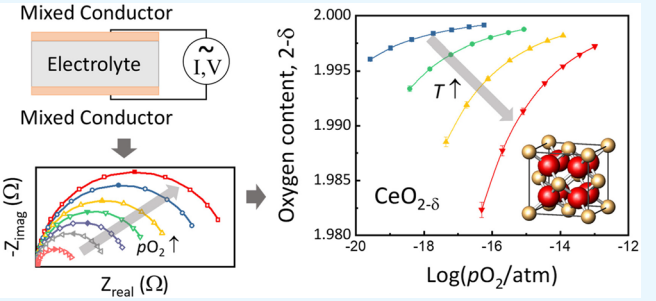

KEYWORDS: *oxygen nonstoichiometry, impedance spectroscopy, chemical capacitance, mixed ion and electron conductor (MIEC), ionic conductivity, ceria, ceria-zirconia*

1. INTRODUCTION

Mixed ion and electron conductors (MIECs) constitute the functional components of many solid state energy conversion devices including solid oxide fuel cells,[1−3] oxygen storage catalysts,[4] solar-driven thermochemical fuel generators,[5−8] and even thermal storage devices.[9] The fundamental thermodynamic property that underlies these applications is the oxygen nonstoichiometry (δ) and in particular its variation with temperature and oxygen partial pressure. Thermogravimetric analysis[10] and coulometric titration[11] are well-established and widely deployed techniques for the measurement of oxygen content and extraction of thermodynamic redox behavior. In recent years, however, electrochemical impedance spectroscopy (EIS) has emerged as a powerful alternative tool for accessing oxygen nonstoichiometry.[12]

Although EIS is typically associated with the measurement of kinetic properties of materials, it is, in fact, effective for determining thermodynamic properties. The approach relies on accurate evaluation of the chemical capacitance of an MIEC. This property is a measure of the chemical energy stored in a material in the form of stoichiometry changes in response to a change in chemical potential, where the latter is induced by a voltage perturbation.[12−15] In an oxide of variable oxygen content, the relevant stoichiometry and chemical potential terms are those of oxygen. The method is particularly well-suited to thin film samples, which are largely incompatible with traditional techniques of measuring nonstoichiometry. Thin films, which are often inherently important in a range of applications, are advantageous over bulk samples for oxygen nonstoichiometry determination due to rapid equilibration in response to changes in temperature and oxygen partial pressure. Thus, the thin film configuration can overcome the need for long measurement times associated with bulk samples, which, beyond the inconvenience of low throughput, can

Received: March 28, 2022
Accepted: April 15, 2022
Published: April 25, 2022

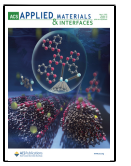

https://doi.org/10.1021/acsami.2c05417
ACS Appl. Mater. Interfaces 2022, 14, 19629−19643

introduce error due to instrument drift and incomplete equilibration.

To date, a handful of studies of model materials (most in a thin film configuration) have demonstrated good-to-quantitative agreement between oxygen nonstoichiometry extracted from EIS and that derived using traditional methods.[16−19] These results have demonstrated the clear connection between capacitance values measured by electrical methods and oxygen content in a nonstoichiometric oxide. However, the analytical methodology has yet to be developed for an arbitrary material, that is, arbitrary defect thermodynamics and interfacial properties. Subtleties arise from the need to distinguish between chemical and surface contributions to capacitance, where only the former is related to the desired thermodynamic properties, and from the absence of a mathematically unique solution for the transformation from chemical capacitance to oxygen nonstoichiometry. Here we present a general methodology for overcoming these challenges. The approach is demonstrated using (i) undoped ceria and (ii) ceria-zirconia of composition $Ce_{0.8}Zr_{0.2}O_{2-\delta}$ (CZO20) in both cases deposited on the pure ionic conductor yttria-stabilized zirconia. These are selected as benchmark materials because their redox thermodynamics, particularly in the case of undoped ceria, are well-known, because the defect solution behavior spans from ideal to nonideal depending on environmental conditions, and because both are MIECs under accessible conditions.[10,20−25] Specifically, ceria is an MIEC under high-temperature (>700 °C), reducing conditions (oxygen partial pressure, $pO_2 \lesssim 10^{-15}$ atm), whereas CZO20 is a mixed conductor across the entire accessible pO_2 range ($1-10^{-20}$ atm) at these same temperatures.

2. THEORY

The interconnection between chemical capacitance, oxygen nonstoichiometry, and impedance response in an MIEC has been reported in several sources.[12,14,15] For completeness, we provide a brief derivation of these interrelationships and expand on the prior literature so as to establish the basis for electrochemical determination of oxygen nonstoichiometry in an arbitrary thin film oxide.

2.1. Chemical Capacitance. The origin of chemical capacitance is readily understood by analogy to the conventional dielectric capacitance, C_{diel}, of a parallel plate capacitor, given by

$$C_{diel} = \frac{\partial q}{\partial E} \tag{1}$$

where q is the charge accumulated on the metal plates to counteract the applied electric potential E. Much like a gradient in electric potential, a gradient or perturbation in chemical potential, μ_k, of species k can induce a change in the quantity of charge stored in the volume of the perturbed material. For a sample with volume V, the charge stored by this species is $q_k = z_k F V c_k$, where c_k is the volumetric concentration of k. Recognizing $\mu_k^* = \mu_k/z_k F$, where F is Faraday's constant and z_k denotes the charge on species k, to be the electrical equivalent to the chemical potential and inserting these definitions into eq 1 yields

$$C_{chem,k} = \frac{\partial q_k}{\partial \mu_k^*} = (Fz_k)^2 V \frac{\partial c_k}{\partial \mu_k} \tag{2}$$

which describes the contribution to the chemical capacitance from a single species. It can be shown that, under the assumption of local electroneutrality, the total chemical capacitance, that is, due to all species, is

$$\frac{1}{C_{chem}} = \sum_k \frac{1}{C_{chem,k}} \tag{3}$$

Where there is one dominant ionic species (ion) and one dominant electronic species (eon), eq 3 becomes

$$C_{chem} = \left(\frac{1}{C_{chem,ion}} + \frac{1}{C_{chem,eon}}\right)^{-1} = F^2 V \left(\frac{1}{z_{ion}^2}\frac{\partial \mu_{ion}}{\partial c_{ion}} + \frac{1}{z_{eon}^2}\frac{\partial \mu_{eon}}{\partial c_{eon}}\right)^{-1} \tag{4}$$

For undoped ceria, these dominant species are most commonly oxygen vacancies and electrons, respectively, and without loss of generality, we refer to these two species hereafter.

Under the further assumptions of local chemical equilibrium and a fixed activity coefficient of oxygen ions of 1, the chemical potential of neutral oxygen, μ_O, is related to that of the oxygen vacancy, μ_{ion}, and the electron, μ_{eon}, according to

$$d\mu_O + d\mu_{ion} + 2d\mu_{eon} = 0 \tag{5}$$

Additionally, the electroneutrality condition requires $2dc_{ion} = dc_{eon} = -2dc_O$. Together, these allow eq 4 to be expressed in terms of neutral oxygen (only) rather than the defect species:

$$C_{chem} = 4F^2 V \left(\frac{d\mu_O}{dc_O}\right)^{-1} \tag{6}$$

The result is identical for an oxide in which oxygen interstitials and electronic holes are the predominant species. Eq 6 can be rewritten in terms of oxygen partial pressure (the quantity that is typically controlled experimentally) by noting that, at equilibrium, the chemical potential of neutral oxygen in the solid and gas phases must be equal such that

$$\mu_O(T, pO_2) = \frac{1}{2}(\mu_{O_2}^0(T) + RT \ln(\hat{p}O_2)) \tag{7}$$

where $\mu_{O_2}^0$ is the chemical potential of gaseous oxygen at standard state (taken to be 1 atm), T is temperature, R is the universal gas constant, and $\hat{p}O_2$ is the oxygen pressure relative to the reference pressure of 1 atm. With this relationship, and noting that the volumetric concentration of oxygen atoms is related to the nonstoichiometry according to $c_O = (m-\delta)/V_m$, where m is the stoichiometric quantity of oxygen in one formula unit of the fully oxidized oxide and V_m is the oxide molar volume, the chemical capacitance becomes

$$C_{chem} = -\frac{8F^2 V\delta}{RTV_m}\left(\frac{d \ln \delta}{d \ln(\hat{p}O_2)}\right) \tag{8}$$

For completeness, we note that for the oxygen interstitial and electron hole case, the volumetric concentration of oxygen atoms is given by $c_O = (\beta + m)/V_m$, where β is the oxygen excess, and eq 8 becomes

$$C_{chem} = \frac{8F^2 V\beta}{RTV_m}\left(\frac{d \ln \beta}{d \ln(\hat{p}O_2)}\right) \tag{9}$$

https://doi.org/10.1021/acsami.2c05417
ACS Appl. Mater. Interfaces 2022, 14, 19629−19643

Written in this form, it is apparent that the chemical capacitance is a measure of the ease of reducibility (or oxidation) of an oxide at a given nonstoichiometry. That is, the larger the C_{chem}, the larger the change in δ (or β) in response to the driving force, $d\ln(\hat{p}O_2)$. Moreover, the term in brackets, which captures the material dependence of this response, can be recognized as the inverse of the thermodynamic factor. It is also noteworthy that, unlike dielectric and interfacial capacitance terms, which scale with area, chemical capacitance scales with volume. As discussed below and as has been demonstrated previously,[16] this difference in scaling behavior, along with differences in absolute value, can be used to deconvolute the relative contributions of these two types of capacitances (interfacial and volumetric) to the total, measured capacitance. The volume-normalized chemical capacitance is defined here as $\bar{\varepsilon}_{chem} = C_{chem}/V$, where the overlying bar is used to emphasize that, while this quantity is independent of material geometry, the units are different from those of the conventional permittivity. It is of some interest to note that when the ionic conductivity, σ_{ion}, is known, and the material is a predominant electronic conductor, the chemical diffusivity can be determined from the chemical capacitance according to[26]

$$D_{chem} = \frac{\sigma_{ion}}{\bar{\varepsilon}_{chem}} \tag{10}$$

2.2. From Chemical Capacitance to Nonstoichiometry. From knowledge of the chemical capacitance as a function of pO_2, the oxygen nonstoichiometry can, in principle, be obtained by integration of eq 8 with respect to pO_2:

$$\delta = \frac{RTV_m}{8F^2V}\int_{pO_2^{ref}}^{pO_2} C_{chem}\, d(\ln \hat{p}O_2) \tag{11}$$

where pO_2^{ref} is a reference oxygen partial pressure at which the nonstoichiometry, δ^{ref}, is known. With high quality data in hand, numerical integration is readily achieved but cannot provide the value of δ at pO_2^{ref}. Accordingly, a common approach is to utilize *a priori* knowledge of the defect chemistry to establish the functional form of $C_{chem}(pO_2)$ and leverage the fact that both C_{chem} and δ^{ref} are zero in the limit $pO_2^{ref} \to \infty$.[16,27] Expanding the chemical capacitance approach to the treatment of MIECs with arbitrary defect chemistry thus requires an additional step of solving the reference-state problem.

Experimentally, it is observed that in many instances, C_{chem} obeys a power-law dependence on $\hat{p}O_2$:

$$C_{chem} = A\hat{p}O_2^n \tag{12}$$

where A and the power law exponent, n, are phenomenological constants.[20] Distinct values of the constants are often detected in different pO_2 regimes, reflecting the distinctive nature of the defect chemistry in these regimes. This results not only because the nature of the dominant defects can change in response to changes in oxygen chemical potential but also because the nature of defect interactions may change as a result of defect ordering or associate formation.[20,22] Regardless of these subtleties, it is expected that C_{chem} and δ will still be zero in the limit $pO_2 \to \infty$. If experiments are carried out at relatively high pO_2, then one can reasonably expect that the measurement captures data close to $\delta = 0$. In such case, one can utilize the highest pO_2 experimental regime for obtaining a set of values for the parameters A and n near the $\delta = 0$ limit, for clarity designated as A^0 and n^0. Insertion of eq 12 into eq 11 then yields

$$\delta = -\frac{RTV_m}{8F^2Vn^0}A^0(\hat{p}O_2)^{n^0} + \delta^{ref} \approx -\frac{RTV_m}{8F^2Vn^0}A^0(\hat{p}O_2)^{n^0} \tag{13}$$

Presuming that the extrapolation to a sufficiently high value of oxygen partial pressure to achieve $\delta \approx 0$ is not extreme, the error introduced by not independently measuring the reference state δ will be small. Treatment of lower pO_2 regions is then achieved by piecewise integration, as demonstrated below.

The generalized result can be compared to that obtained in the limit of ideal solution behavior. For undoped ceria undergoing reduction, the relevant defect reaction is[20]

$$O_O^x \leftrightarrow \frac{1}{2}O_2(g) + V_O^{\bullet\bullet} + 2e' \tag{14}$$

Under ideal solution behavior and the condition of electroneutrality, the law of mass action implies[20]

$$\delta = \left(\frac{K_{red}}{2}\right)^{1/3}\hat{p}O_2^{-1/6} \tag{15}$$

where K_{red} is the equilibrium constant. Inserting eq 15 into eq 8 yields a simplified expression for the chemical capacitance:

$$C_{chem} = \frac{4F^2V}{3RTV_m}\delta \tag{16}$$

The above implies that if ideal solution behavior is obeyed, then the experimentally obtained C_{chem} will display a $pO_2^{-1/6}$ power law dependence, and eq 16 can be used to directly obtain the nonstoichiometry, circumventing the requirement of identifying a reference state as expressed in eq 11. In practice, however, under many conditions, undoped ceria does not display ideal solution thermodynamics,[20] necessitating assessment of the reference state.

It is of value to compare the situation to doped ceria, for which analogous expressions apply. For example, when the dopant is a trivalent species, D, the nonstoichiometry due to Ce reduction (i.e., in excess of that due to doping) is[20]

$$\delta = \left(\frac{K_{red}}{X_D}\right)^{1/2}\hat{p}O_2^{-1/4} \tag{17}$$

where X_D is the fraction of dopant on the Ce site. Accordingly, the chemical capacitance becomes

$$C_{chem} = \frac{2F^2V}{RTV_m}\delta \tag{18}$$

and in this case C_{chem} will display a $pO_2^{-1/4}$ power law dependence when ideal solution thermodynamics is obeyed. Examples of this behavior have been observed for $Ce_{0.8}Sm_{0.2}O_{1.9-\delta}$[16] and $Ce_{0.9}Pr_{0.1}O_{1.95-\delta}$[17] (the latter in the regime in which all of the Pr is reduced to the 3+ oxidation state). Accordingly, the nonstoichiometry can be directly computed by inverting eq 18. Finally, it is noted that as expected, eqs 15 and 17 are both consistent with the statement that δ (and hence C_{chem}) is zero in the limit $pO_2 \to \infty$.

2.3. Chemical Capacitance from EIS. The extraction of chemical capacitance from electrochemical impedance data is facilitated by mapping the physical response of the system to an appropriate equivalent circuit. The measurement geometry used here is that in which dense films of the MIEC sample are

https://doi.org/10.1021/acsami.2c05417
ACS Appl. Mater. Interfaces 2022, 14, 19629−19643

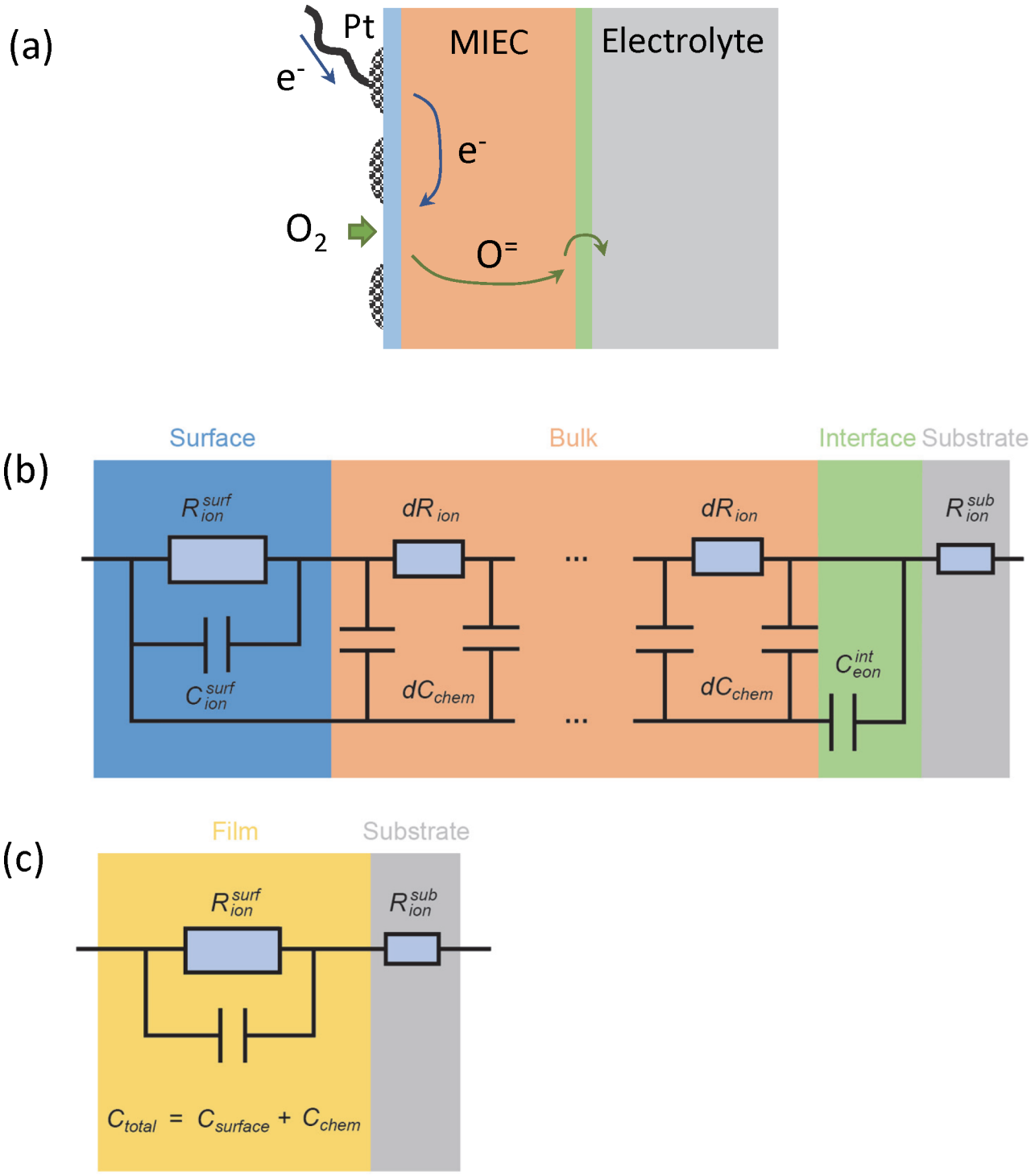

Figure 1. Representation of the electrochemical processes occurring on a variable valence, mixed ion and electron conducting (MIEC) thin film oxide (grown on an oxygen ion conducting electrolyte) undergoing changes in oxygen stoichiometry in response to an electrical driving force: (a) schematic of the physical steps; (b) equivalent electrical circuit when the electronic resistance of the film is negligible and the ionic resistance is non-negligible; (b) equivalent electric circuit when the ionic resistance is also negligible.

deposited on both sides of an electron-blocking YSZ electrolyte substrate, and porous metal electrodes are applied atop of the dense films to serve as current collectors. Charge transport across this system, Figure 1a, occurs via a series of (reversible) steps:[26,28] (1) surface reaction at the MIEC|gas interface (which may be catalyzed at the triple phase boundaries at which the porous metal is in contact with this interface), (2) mixed transport of electrons and oxygen ions through the dense MIEC film, (3) charge transfer/incorporation at the MIEC|electrolyte interface, and (4) ion transport through the electrolyte. The symmetry of the system implies the simultaneous occurrence of the reverse reactions (on the opposite electrode, and upon reversing the voltage during A.C. measurements).

It has been shown elsewhere that the impedance response of an MIEC that obeys the condition of electroneutrality can be

https://doi.org/10.1021/acsami.2c05417
ACS Appl. Mater. Interfaces 2022, 14, 19629−19643

rigorously mapped to a transmission line equivalent circuit comprising an ionic path in parallel with an electronic path, with differential resistance units (dR_{ion} and dR_{eon}, respectively) linked by differential units of chemical capacitance (dC_{chem}).[12,14] When the electronic conductivity in the MIEC is much higher than that of the ionic conductivity, the electronic resistance terms can be dropped. Phenomenological treatment of the two interfacial steps along with assignment of an ohmic resistance to the electrolyte (R_{ion}^{sub}) yields the equivalent circuit shown in Figure 1b.[26,28] Here, the reaction at the MIEC|gas interface is assigned a single (RC) parallel circuit (with terms R_{ion}^{surf} and C_{ion}^{surf}), the incorporation of electrons from the metal into the MIEC and of ions from the MIEC into the electrolyte are treated as barrierless, and the electronic rail is terminated at the electrolyte with a capacitor (C_{eon}^{int}). The analytical expression for this circuit has been given previously[26,28] and is reproduced here in the Appendix, along with additional discussion. The impedance spectrum presented on the complex plane (Nyquist plot) is characterized by a primary arc associated with the electrochemical reaction and a high frequency diffusion feature. Under favorable conditions, impedance fitting yields the following parameters: C_{chem}, R_{ion}, C_{ion}^{surf}, R_{ion}^{surf}, R_{ion}^{sub}, and C_{eon}^{int}. Although not relevant to the bulk properties of interest here, it is noted that the very large value of C_{chem} typically obscures any features of the surface reaction response that would indicate a multistep process with steps of differing time constants. In the present work, where the equivalent circuit shown in Figure 1b applied, C_{eon}^{int} was so small as to be undetermined and could be ignored with no impact on the derived values of the desired terms, C_{chem} and R_{ion}. The analytical expression for the condition of zero interfacial electronic capacitance is also provided in the Appendix.

If the ionic resistance through the film is very small relative to the surface reaction resistance (as encountered, in particular, in very thin films), the ionic resistance terms become negligible, resulting in the equivalent circuit shown in Figure 1c,[16] where C_{tot}^{surf} is the sum of the two interfacial capacitances, C_{ion}^{surf} and C_{eon}^{int}. In this case, the electrochemical behavior is simply described by the resistor R_{ion}^{sub} in series with a parallel subcircuit of $2R_{ion}^{surf}$ and $1/2(C_{tot}^{surf} + C_{chem})$, where the factors of 2 and 1/2 arise because of the sample symmetry with films on either side of the substrate. In the thin film limit, the diffusional feature is thus lost, and all the capacitance terms become lumped into a single parameter. The term C_{chem} can be recovered from this summed quantity by varying film thickness because chemical capacitance scales with thickness (due to its proportionality to volume), whereas the interfacial capacitance contributions are independent of film thickness. Recognizing the geometric distinctions, the area-normalized total capacitance, $\tilde{C}_{tot}$, is given as

$$\tilde{C}_{tot} = \frac{C_{tot}}{A} = \tilde{C}_{tot}^{surf} + \bar{\varepsilon}_{chem} L \tag{19}$$

where $\tilde{C}_{tot}^{surf}$ is the area-normalized surface (or interfacial) capacitance. By measuring the electrochemical response of a series of films with differing L and applying this expression, one can deconvolute the chemical and interfacial contributions to the measured capacitance.[16]

The treatment here ignores the possible contribution of the bulk capacitance of the MIEC film to the overall behavior. This is justified by recognizing that the area normalized dielectric capacitance of a ceria film, with relative dielectric constant[29] of ~35 and thickness of 170 nm (corresponding to the thinnest film studied here) is just $\sim 10^{-7}$ F cm^{-2}. This is more than 3 orders of magnitude smaller than the smallest capacitance observed in the present study.

3. EXPERIMENTAL METHODS

3.1. Sample Preparation and Characterization. Films were grown by pulsed laser deposition, for which targets were fabricated in-house by conventional ceramics processing routes using cerium(IV) oxide (Sigma-Aldrich, 1306−38−3, 99.995% metals basis) and zirconium(IV) oxide (1314−23−4, 99.99% metals basis). For the preparation of the CZO20 target, appropriate quantities of the powders were ball-milled in ethanol using yttria-stabilized zirconia (YSZ) milling media, then retrieved and gently dried. Discs were formed by uniaxial compaction and then sintered at 1500 °C for 10 h, yielding targets with >95% theoretical density. Films were grown using a PLD/MBE 2300 (PVD Products, 248 nm KrF laser, 200 mJ/pulse, 10 Hz repetition rate, with a calibrated growth rate of 4 nm/min) on double-side polished YSZ substrates (MTI, 10 × 10 × 0.5 mm^3, 2SP, YSZa101005S2). The substrate temperature was fixed at 700 °C (calibrated) and the oxygen pressure in the chamber set at 10 mTorr. Upon completion of the deposition, the chamber was vented to 100 Torr oxygen pressure and cooled at a rate of 5 °C/min. The growth procedure was immediately repeated on the opposite side of the substrate to create symmetric samples. Four different thicknesses of ceria films were prepared: 170, 630, 840, and 1050 nm (on each side), whereas three films of CZO20 with the following thicknesses were grown: 230, 460, 690 nm (on each side). The films each covered an area of 7.5 × 10 mm^2 on the 10 × 10 mm^2 substrates. Film thickness was measured for selected samples using contact stylus profilometry (Veeco Dektak 150).

Coupled 2θ−ω X-ray diffraction scans of the crystals grown on the single-crystal YSZ revealed only peaks attributable to the substrate and the ceria or ceria-zirconia film, as shown in the representative results for the 630 nm thick ceria film and the 230 nm thick ceria-zirconia film (Figure 2). While the latter is fully oriented along the

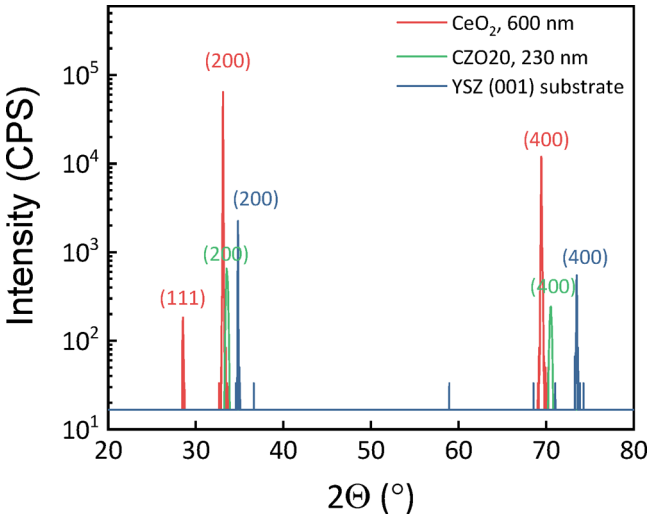

Figure 2. 2θ−ω coupled scan of a 600 nm film of ceria and a 230 nm film of CZO20 deposited on a (001) oriented YSZ substrate.

(100) direction, matching the substrate orientation, the ceria film shows a small (111) peak, indicating the presence of a small concentration of misoriented domains. In prior studies using similar growth conditions, complete epitaxy was achieved in relatively thin films (220 nm) for Zr content of up to 48 cat %.[32] Because chemical capacitance is a bulk property, film orientation does not affect the measurement,[16] whereas the near-epitaxial nature suggests a minimal role for grain boundaries. The lattice parameters of the two film materials were found to be 5.409 ± 0.001 Å (ceria) and 5.339 ± 0.006

https://doi.org/10.1021/acsami.2c05417
ACS Appl. Mater. Interfaces 2022, 14, 19629−19643

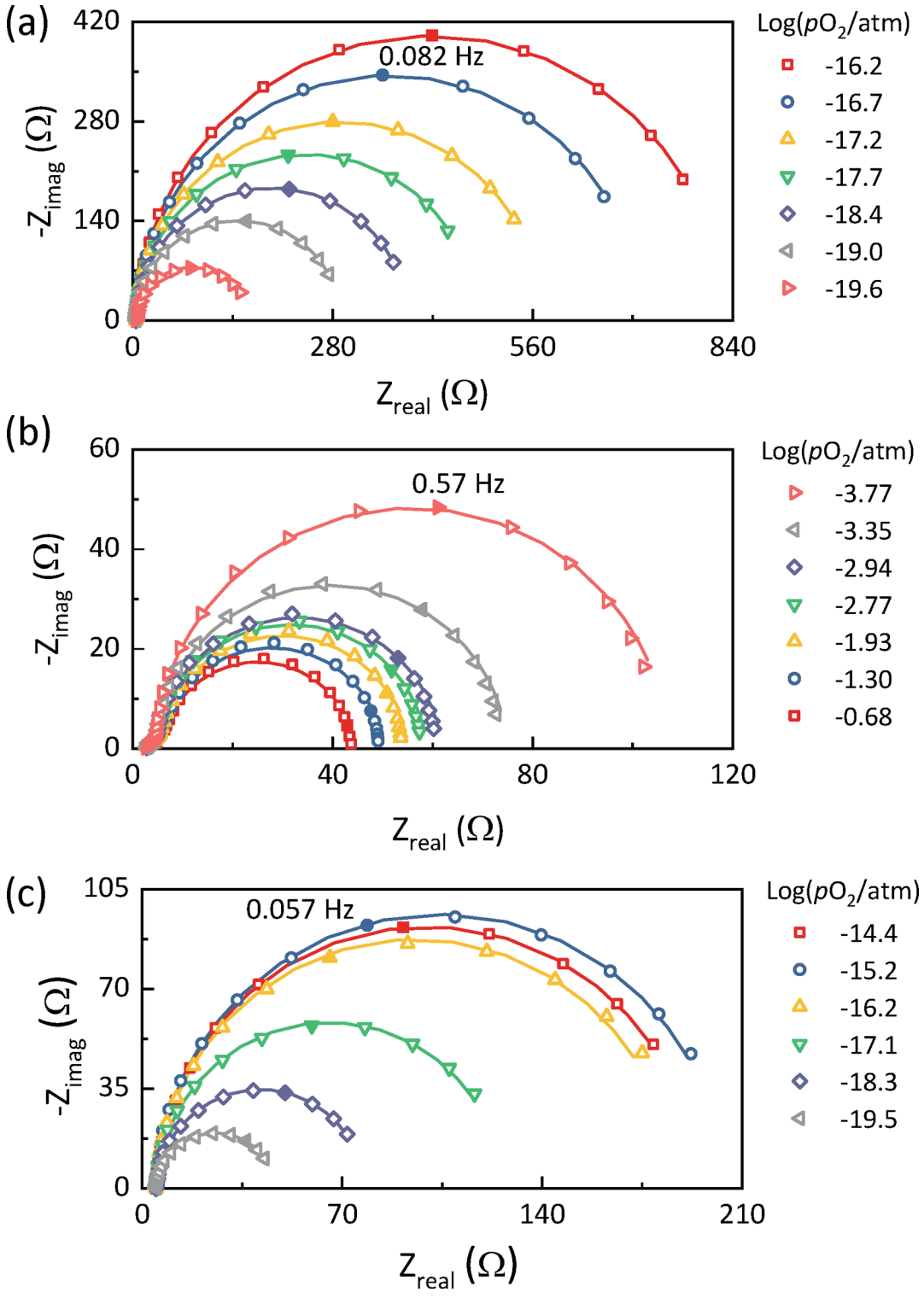

Figure 3. Selected impedance spectra representative of the three sets of conditions of this work, where lines are fits and data points are experimentally measured values: (a) 1050 nm ceria under reducing conditions (T = 750 °C); (b) 690 nm CZO20 under oxidizing conditions (T = 800 °C); and (c) 230 nm CZO20 under reducing conditions (T = 746 °C). In all cases, films are grown on (001) YSZ substrate. The ohmic offsets, including those barely visible in panel a, agree with the known ionic resistivity of YSZ (see SI).

Å (CZO20), matching reasonably well the values of the bulk materials, 5.407 and 5.356 Å, respectively.[30]

3.2. Electrochemical Measurements. Pt (Heraeus, Item# CL11−5349) was brush painted on both sides of the film|YSZ|film symmetric cell and cured for 2 h at 900 °C to obtain a porous, interconnected current collector over the entire film area. The sample was mechanically contacted by Pt clips and placed in a gastight quartz reactor through which gas was supplied. In the oxidizing regime, the oxygen partial pressure (pO_2) was controlled in the range from 10^{-4} to 0.2 atm by mixing O_2 and Ar. In the reducing regime, pO_2 control was achieving by mixing 3% H_2 (balance Ar) with N_2, and then passing the diluted H_2 gas stream through a water bubbler held at 21 °C to attain 2.3% H_2O. The pO_2 realized in the reactor was determined *in situ* using a YSZ-based oxygen sensor (Setnag,

https://doi.org/10.1021/acsami.2c05417
ACS Appl. Mater. Interfaces 2022, 14, 19629−19643

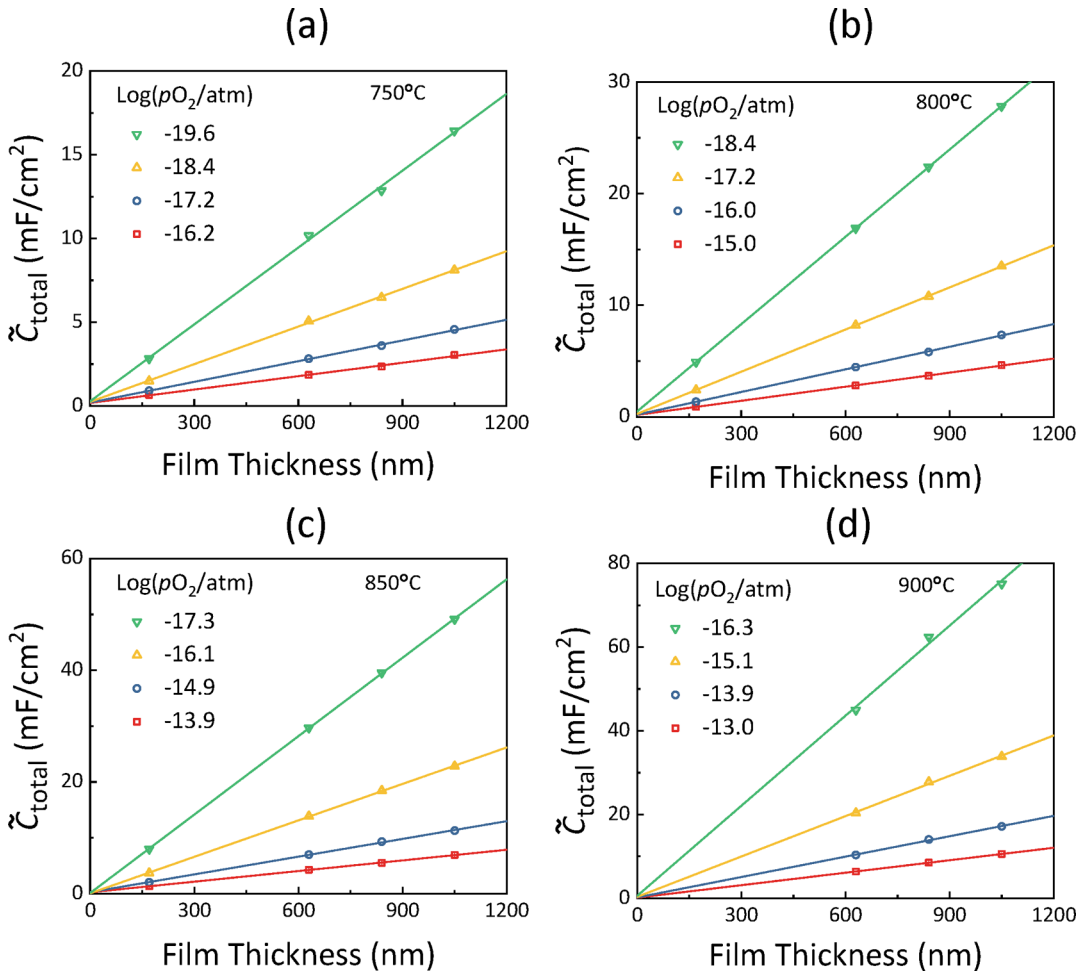

Figure 4. Total capacitance (area-normalized) of undoped ceria measured under reducing conditions and shown as a function of film thickness at (a) 750 °C; (b) 800 °C; (c) 850 °C; and (d) 900 °C. Lines are linear fits used for extracting the (small) interfacial contribution to the total capacitance.

MicroPoas). The AC impedance response of the cells was measured between 750 and 900 °C using a Biologic SP-200 impedance analyzer over a frequency range falling between 1 mHz to 10 kHz (adjusted to match material response characteristics) and a 30-mV perturbation voltage under zero bias. The samples were equilibrated for 30 min at each pO_2 condition before data collection. For each measurement temperature, after sweeping through the range of pO_2 values, the initial gas condition was re-examined to confirm the absence of sample evolution over the measurement period. Undoped ceria was measured under reducing conditions (pO_2 ~10^{-13} to ~10^{-20} atm), whereas CZO20 was measured under both these reducing conditions and relatively oxidizing conditions (pO_2 ~$10^{-0.5}$ to ~10^{-4} atm), where the latter conditions are hereafter referred to simply as 'oxidizing'. Data were analyzed using in-house developed code written in Python (freeware) or, in the case of the conventional R(RQ) equivalent circuit, using the commercial software package ZView (Scribner Associates) with statistically insignificant differences for the latter circuit between the results of analysis using the in-house and commercial codes.

4. RESULTS AND DISCUSSION

Representative impedance spectra for CeO_2 measured under reducing conditions (t = 1050 nm, T = 750 °C), CZO20 under oxidizing conditions (t = 690 nm, T = 800 °C), and CZO20 under reducing conditions (t = 230 nm, T = 746 °C) are shown on the complex plane (Nyquist plots) in Figure 3 (see also Figure S1). The spectra are consistent with the equivalent circuits described in Figure 1; the full set of fit parameters associated with these spectra is provided in the Supporting Information (SI) Table S1 and Figure S2. A small offset along the real axis that is independent of both pO_2 and film thickness is observed at the high-frequency limit for all measurements. This offset corresponds to the ionic resistance of the YSZ substrate from which a conductivity of 0.025 S/cm is obtained at 800 °C, in good agreement with the well-documented properties of this material.[31] The dominant feature of these spectra is the large pO_2-dependent arc, where the pO_2 sensitivity immediately reveals that this response reflects the properties of the MIEC electrodes. Although the magnitude of this arc, which varies quite significantly with pO_2, is a measure of the rate of the electrochemical reaction on the MIEC surface, the capacitance, which is the property of interest here, is embedded in the frequency dependence. Though more subtle, the pO_2 influences this aspect of the spectra as well. For the measurement of CZO20 under oxidizing conditions, a small but nevertheless significant feature attributable to the diffusional response appears at high frequency, which is absent in the other spectra.

4.1. Ceria under Reducing Conditions. The impedance response of the undoped ceria films could, under all conditions, be satisfactorily described by an $R(RQ)$ circuit, where Q represents a constant phase element with impedance

https://doi.org/10.1021/acsami.2c05417
ACS Appl. Mater. Interfaces 2022, 14, 19629−19643

$Z_Q = Q^{-1}(i\omega)^{-n_q}$, in which Q is a constant, $i = \sqrt{-1}$, ω is frequency, and n_q is a constant between 0 and 1 (not be confused with the power law exponent in eq 12). In all cases, n_q was found to be ≥0.95 and the equivalent capacitance was accordingly obtained according to $C = Q^{1/n_q}R^{1/n_q-1}$. The impedance behavior is consistent with the equivalent circuit presented in Figure 1c. Shown in Figure 4 are plots of $\tilde{C}_{tot}$ as a function of film thickness. Good linearity is observed under all measurement conditions. Moreover, the intercept is close to zero for all cases, indicating that the bulk chemical capacitance dominates the capacitive response over the surface capacitance, even in the thinnest film (170 nm) studied. This is due to a high concentration of oxygen vacancies under reducing conditions (eq 8). From the small but nonzero intercept, it is possible to estimate the surface capacitance. The summary results, Figure 5a, indicate that the sensitivity of $\tilde{C}_{tot}^{surf}$ to temperature and oxygen partial pressure falls below the uncertainty in the measurement. Such behavior suggests low sensitivity of the surface redox state (in which the surface is highly reduced) to these state variables, as has been deduced on the basis of direct measurements of the Ce^{3+} concentration in the surface regions of ceria-based films.[32−34]

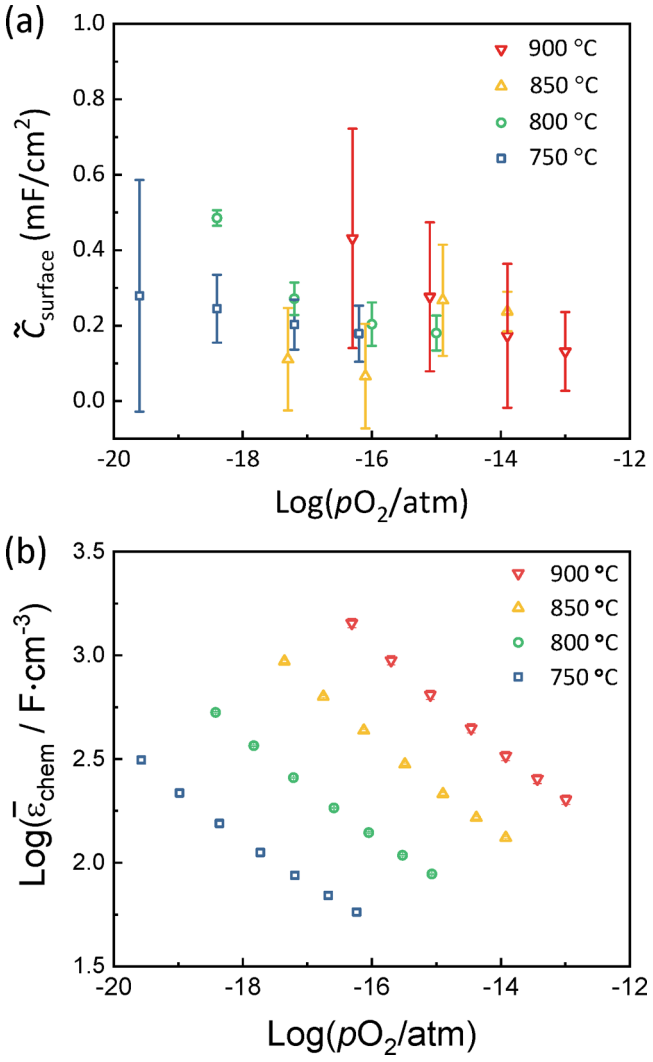

Figure 5. Deconvoluted capacitance properties of undoped ceria measured under reducing conditions and shown as functions of oxygen partial pressure: (a) interfacial capacitance (area-normalized) shows a weak dependence on oxygen partial pressure and temperature; and (b) chemical capacitance (volume-normalized), with nonlinear behavior in the double-logarithmic plot, reveals the nonideal solution thermodynamics of undoped ceria.

The chemical capacitance, Figure 5b, obtained after subtracting the surface capacitance from the total capacitance, displays exactly the behavior that is expected for an n-type MIEC, increasing with increasing temperature and with decreasing oxygen partial pressure as a consequence of the rising oxygen nonstoichiometry. If ideal solution behavior were to be obeyed, a slope of −1/6 would be expected in the double-logarithmic plot shown. Instead, observed here is a slope that gradually changes from −0.2 to −0.3 as pO_2 decreases, indicating nonideality in the solution properties. While this insight is not new for ceria,[22,35] it is precisely this feature that precludes direct analytical integration of eq 8 to obtain the oxygen nonstoichiometry. Accordingly, a two-part integration approach was implemented as alluded to above. Specifically, first, a fit was performed to the three highest pO_2 data points to determine $A^0(T)$ and $n^0(T)$, eq 12. The values were then used to compute δ according to eq 13 (right side) at the highest pO_2 of measurement, corresponding specifically to 8.4×10^{-4} at 750 °C and $10^{-16.24}$ atm, 1.2×10^{-3} at 800 °C and $10^{-15.07}$ atm, 1.8×10^{-3} at 850 °C and $10^{-13.92}$ atm, and 2.8×10^{-3} at 900 °C and $10^{-12.99}$ atm. With these reference values in hand, the $C_{chem}(pO_2)$ curves were numerically integrated, eq 11, from high to low pO_2, to generate the nonstoichiometry profiles. The evidently small δ values at the reference conditions suggest the errors introduced by the approximation inherent to this approach are small, as verified below.

The resulting oxygen stoichiometry profiles are shown in Figure 6a. These data were then further utilized to extract the relative partial molar enthalpy $\Delta\bar{H}_O^0$and the relative partial molar entropy $\Delta\bar{S}_O^0$ of oxygen in ceria using a van't Hoff analysis.[23] In this method, the set of (T, pO_2) pairs that gives rise to a given δ is presented on an Arrhenius plot, and the slope and intercept are used to determine, respectively, the enthalpy and entropy at the specified δ (Figure S3). These terms are related to the enthalpy and entropy of the reduction reaction, eq 14, according to $\Delta\bar{H}_O^0 = -1/2\Delta_{red}H^0$ and $\Delta\bar{S}_O^0 = -1/2(\Delta_{red}S^0 + S_{config})$, where S_{config} is the configurational entropy of defective solid.[20,36] The thermodynamic functions so obtained are presented in Figure 6b for the very narrow range of ceria stoichiometries from $CeO_{1.9935}$ to $CeO_{1.9980}$ for which at least 3 measurements are available. The oxygen content derived from the electrochemical measurements, Figure 6a, is in good agreement with the results obtained by thermogravimetric analysis (TGA).[10] The small disagreement at the lowest temperature of measurement (800 C), along with the limited temperature range over which electrochemical data were collected, results in a noticeable discrepancy in the thermodynamic terms from the two types of measurements at very low δ, Figure 6b. Beyond comparison to the Panlener results, the partial molar enthalpy value of −472 ± 5 kJ/mol-O obtained in this work at δ = 0.0065 falls within the range of about 450 to 500 kJ/mol-O reported in the literature at this δ.[37] Similarly, the entropy value of −263 ± 5 J/K/mol-O falls within the literature range of 240 to 290 J/K/mol-O (again, at δ = 0.0065).[37] The results thus demonstrate that the electrochemical approach, which yielded the full set of data shown in Figure 6 within 24 h as compared to several (>4) days required for TGA measurements,[23] can be applied to

https://doi.org/10.1021/acsami.2c05417
ACS Appl. Mater. Interfaces 2022, 14, 19629−19643

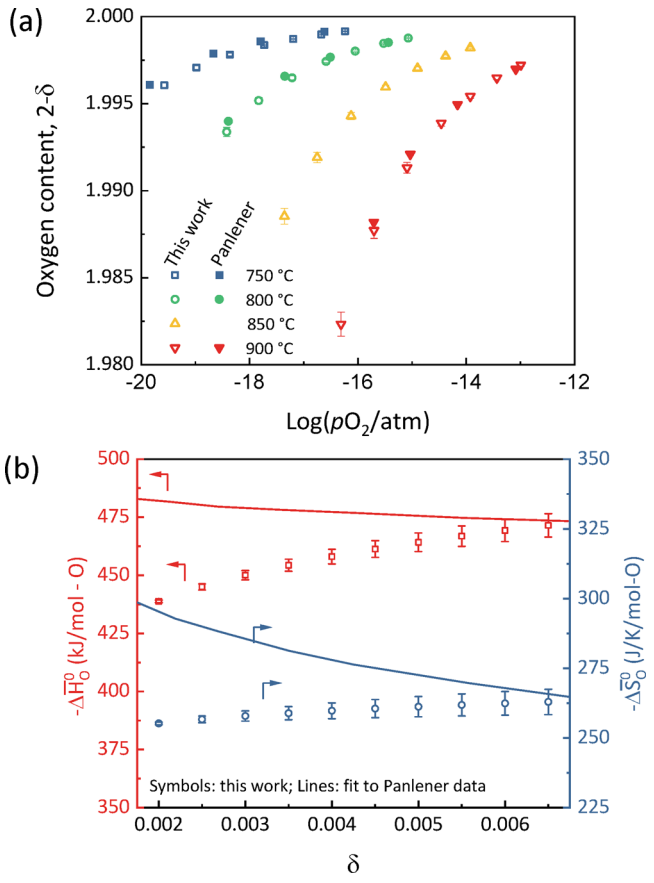

Figure 6. Thermochemical properties of undoped ceria under reducing conditions deduced from chemical capacitance: (a) oxygen stoichiometry as a function of oxygen partial pressure at the temperatures indicated; and (b) standard partial molar enthalpy and standard partial molar entropy of oxygen in the oxide (see Figure S3 for details of analysis). Results are compared to those of Panlener[10] obtained by thermogravimetry.

determine accurate thermodynamic data even in the absence of a defect chemical model.

4.2. CZO20 under Oxidizing Conditions. The clear emergence of a high-frequency diffusional feature in the impedance spectra of CZO20 under oxidizing conditions, particularly for the thicker films (460 and 690 nm), motivated analysis of these results in the context of the equivalent circuit presented in Figure 1b. An example of the fitting results is presented in Figure 7 (t = 690 nm, T = 800 °C), revealing the success of the model in capturing the high frequency behavior. A challenge emerges, however, in terms of capturing the dispersion effects, which are typically represented by replacing capacitors with constant phase elements, and then computing the effective capacitance from the fit parameters. Here, it was found that the impedance data were indeed best fit using a modification to eq A.1 in which the capacitor representing the chemical capacitance was replaced by a constant phase element (this fit is shown in Figure 7). Such an analysis, which yielded an n_q of at least 0.94 in all cases, was specifically required for obtaining meaningful fits from the thinnest films at the lowest pO_2 conditions. The modified expression was used for determining R_{ion}, whereas C_{chem} was obtained by fitting directly to eq A.1 (or A.2) using an ideal capacitor, avoiding the need to develop a formalism for determining the effective capacitance.

Shown in Figure 8 are the area-normalized quantities obtained for the representative temperature of 800 °C. It is emphasized that these parameters are determined directly from the equivalent circuit fitting, without an additional step of deconvoluting surface contributions to the capacitance. The linearity with thickness and an intercept of approximately zero from the linear fits together provide a self-consistency check on the approach. Alternative methods for determining the ionic conductivity in MIECs are available but are challenging when the ionic transference number is low.[38,39]

The volumetric chemical capacitance, determined using only the data from the thickest film for which n_q was $\geq$ 0.97, is summarized in Figure 9a as a function of pO_2. This property displays a fixed slope in the double-logarithmic plot, with a value close to −1/8, Figure 9a. The fixed n (and A), as well as the relatively large pO_2 values of the measurements, enables the use of eq 13 (right side) directly to determine the nonstoichiometry. The results, Figure 9b, are slightly larger those in the literature derived from TGA measurements[40] but generally lie within two standard deviations of the large uncertainties associated with the latter. Because of the high sensitivity of the electrical response to small changes in oxygen content, the present results display much smaller uncertainty. Accurate measurements under oxidizing environments are a challenge for thermogravimetry because the mass loss is small under these low δ conditions. A power law exponent of close to −1/6 derived in several studies[24,41] in principle signifies that CZO20 obeys ideal solution behavior under oxidizing conditions. If such behavior is obeyed, then the non-stoichiometry is given directly by inverting eq 16, the results of which are also shown in Figure 9b. The deviation in this value from both the literature TGA results and from the electrochemical δ computed using eq 13 is notable. The discrepancy may reflect the limits of the electrochemical approach, or it may reflect differences due to the presence of trace impurities, which can dominate behavior when intrinsic defect concentrations or low, or it may reflect an overlooked feature of CZO (i.e., it does not behave ideally), revealed here by the sensitivity of the electrochemical measurements. As in the case of undoped ceria, due to the narrow temperature range of the measurements, even small discrepancies in absolute nonstoichiometry (between the present work and prior studies) manifest as large discrepancies in enthalpy and entropy values. Shown for example in Figure 9c is the $K_{red}(T)$ computed assuming ideal solution behavior at the condition $\log(pO_2/\text{atm}) = -3.77$. While the values of the equilibrium constant are within error of the prior literature,[40] the enthalpy and especially entropy values are smaller (−207 kJ/mol-O and −2 J/K/mol-O, respectively). Nevertheless, the present work supports prior findings of a dramatic decrease in the magnitude of the reduction enthalpy in ceria (which as noted above exceeds 450 kJ/mol-O at small δ) upon introduction of zirconia.[40,42]

From the ionic resistance and chemical capacitance, Figure 8, the ionic conductivity and chemical diffusivity are readily obtained, Figure 10, where the latter is derived according to eq 10. The ionic conductivity found here, $\sim 10^{-4}$ S/cm at 900 °C under air, is comparable in magnitude to that reported by Chiodelli et al.[21] These authors obtained their result from the total conductivity of CZO20 in combination with its ionic transference number measured using an oxygen concentration cell. Others have attempted to infer the ionic conductivity from total conductivity measurements as a function of oxygen partial

https://doi.org/10.1021/acsami.2c05417
ACS Appl. Mater. Interfaces 2022, 14, 19629−19643

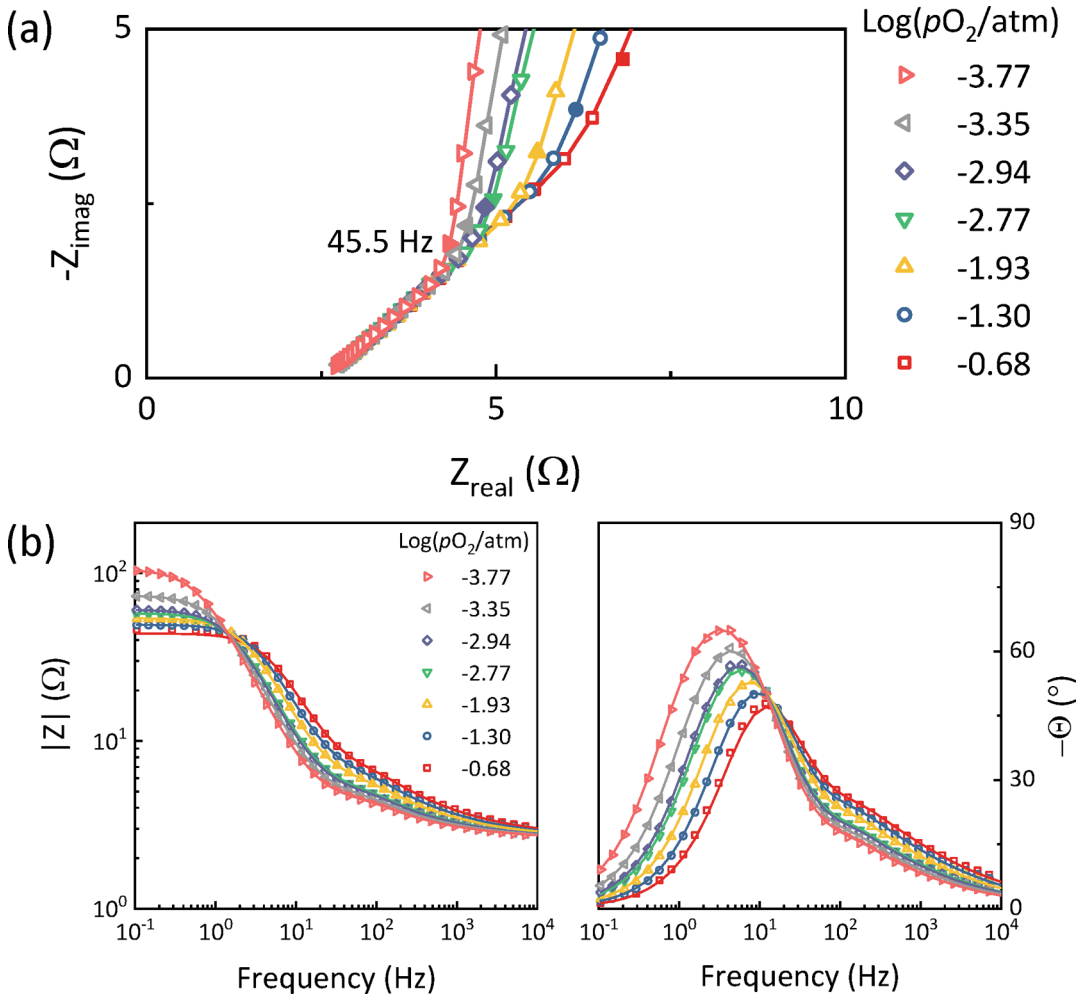

Figure 7. Impedance of CZO20 690 nm film measured under oxidizing conditions at 800 °C, where lines are fits and data points are experimentally measured values: (a) expanded view of the high-frequency region showing diffusional feature; (b) magnitude and phase of impedance as functions of frequency. The fit is realized using the equivalent circuit shown in Figure 1b and simulates the experimental data well, including the high frequency diffusional feature.

pressure using defect chemical models.[21,25,43] In the present study, the result is obtained directly as part of a conventional impedance measurement, and moreover with little scatter in the data. While a detailed investigation of the transport properties of CZO20 is beyond the scope of this work, it is of some interest that the ionic conductivity displays a power law exponent of ~−1/8, which is similar to the power law exponent measured for the chemical capacitance. Eq 10 thus yields a chemical diffusivity that is, to a first approximation, independent of oxygen partial pressure. This result implies that the chemical diffusivity is independent of the oxygen vacancy concentration, behavior that results when the chemical diffusivity (D_{chem}) is dominated by the oxygen vacancy diffusivity ($D_{V_O^{\bullet\bullet}}$) and when the vacancy diffusivity is itself independent of oxygen vacancy concentration. For undoped reduced ceria, electroneutrality implies $c_{e'} = 2c_{V_O^{\bullet\bullet}}$, where $c_{e'}$ and $c_{V_O^{\bullet\bullet}}$ are the volumetric electron (or Ce^{3+}) and oxygen vacancy concentrations, respectively, which in turn implies $D_{chem} \approx 3D_{V_O^{\bullet\bullet}}$.[44] Given the small variation in oxygen vacancy concentration over the pO_2 measurement range, it is not surprising that $D_{V_O^{\bullet\bullet}}$ (which does not explicitly dependent on $c_{V_O^{\bullet\bullet}}$) is approximately constant.

4.3. CZO20 under Reducing Conditions. Under reducing conditions, consistent with the increase in ionic conductivity noted in Figure 10a as pO_2 falls, the diffusion feature is absent from the impedance data (Figure 3c). Accordingly, the spectra were analyzed using the simple $R(RQ)$ circuit, and again, n_q was in all ≥0.95. Moreover, because the chemical capacitance dominates the surface contribution at reducing conditions (as shown for undoped ceria in Figure 4), data from multiple films were not required. Accordingly, data collection was largely limited to the 230 nm film, with selected measurements of the 460 nm film performed for validation of the assumption of a negligible interfacial contribution. The volumetric capacitance measurements under the reducing conditions are summarized in Figure 11, where it is evident that the results for the two different thickness films are in good agreement.

Significantly, the power law exponent for these conditions is substantially smaller in magnitude in the highly reducing regime (~−1/16) than in the oxidizing region, where it was observed to be close to −1/8. Such behavior has been previously noted in both conductivity and TGA studies.[24,40,42] The shallow slope, given its disagreement with the behavior at higher pO_2, immediately implies that the chemical capacitance cannot be extrapolated to the $pO_2 \rightarrow \infty$ ($\delta \rightarrow 0$) limit to

https://doi.org/10.1021/acsami.2c05417
ACS Appl. Mater. Interfaces 2022, 14, 19629−19643

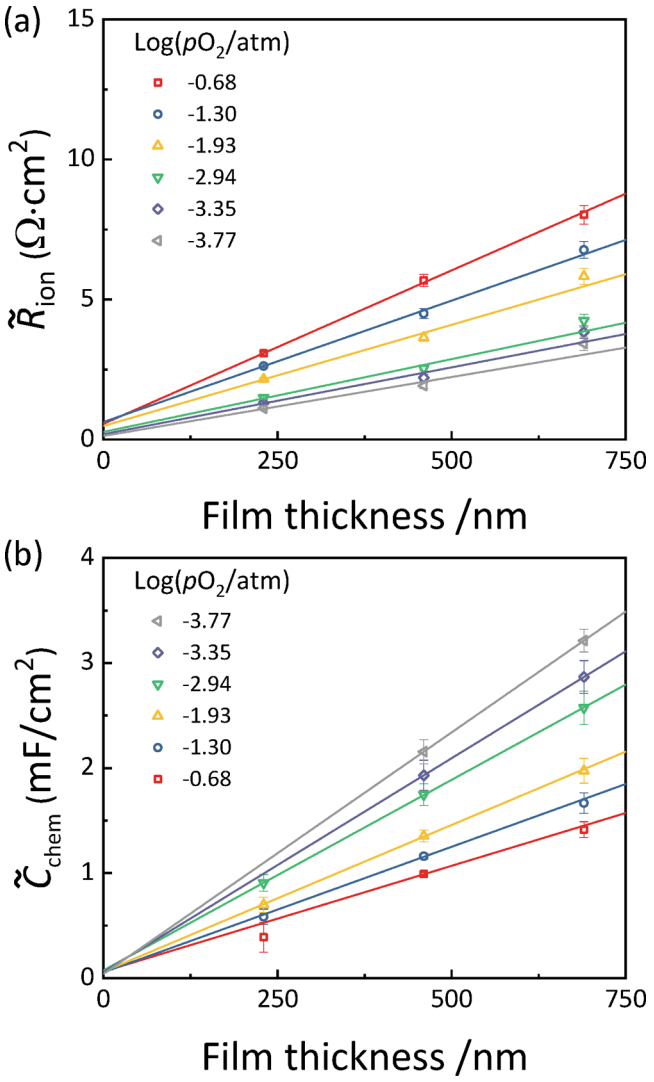

Figure 8. Thickness dependence of the electrochemcial properties of CZO20 films measured under oxidizing conditions at 800 °C and determined by fitting to impedance data using the equivalent circuit model shown in Figure 1b: (a) ionic resistance (area-normalized), and (b) chemical capacitance (area-normalized). The linearity of the results supports the validity of the impedance model [data shown only for conditions under which all three film thicknesses were evaluated].

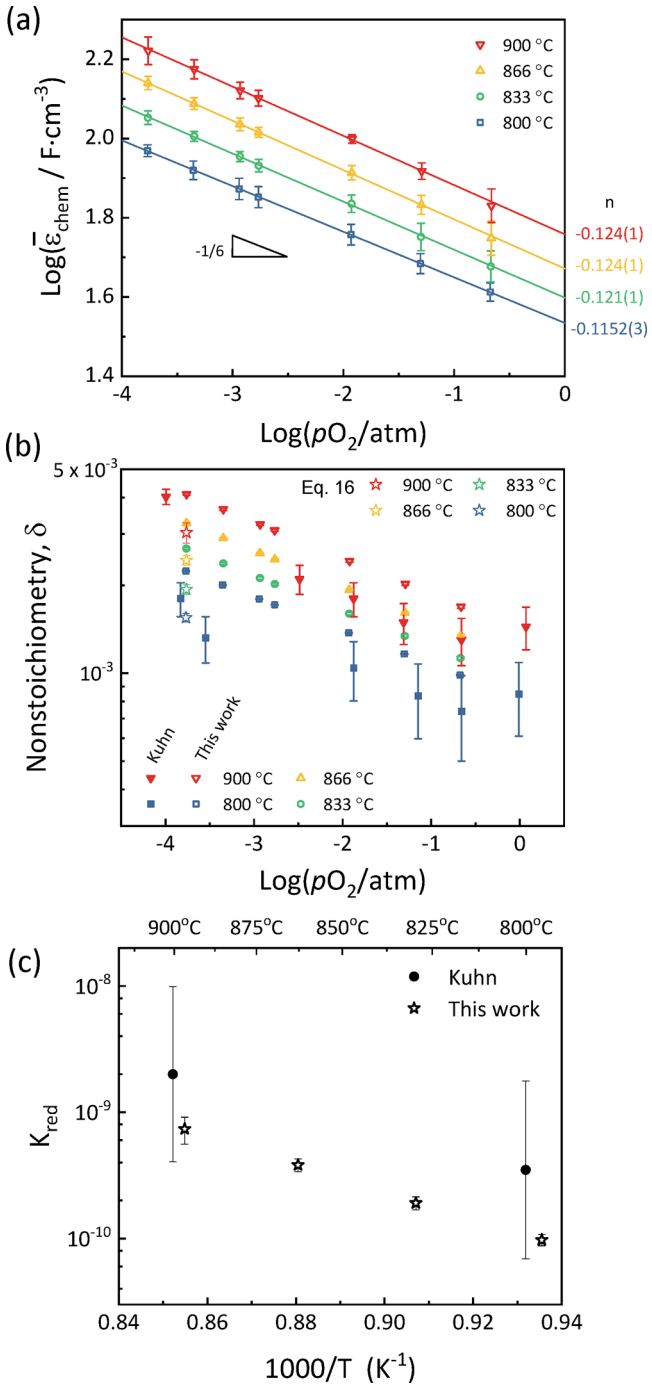

Figure 9. Thermochemical properties of CZO20 under oxidizing conditions deduced from impedance analysis: (a) chemical capacitance (volume-normalized) as a function of oxygen partial pressure at the temperatures indicated; (b) oxygen nonstoichiometry as a function of oxygen partial pressure at the temperatures indicated, determined by direct integration of chemical capacitance (eq 13) and by direct calculation (eq 16) at the lowest oxygen partial pressure condition; and (c) equilibrium reduction constant (eq 15) obtained from the starred data points in panel b. The number in parentheses following the value of the power law exponent in panel a is the fitting uncertainty in the last digit. The results are in reasonable agreement with the work of Kuhn et al.[40] obtained by thermogravimetry, shown in panels b and c, while being subject to much smaller uncertainty.

determine the absolute oxygen content according to eq 13. The problem was treated here by extrapolating the data measured in the high pO_2 region to meet the data in the low pO_2 region, Figure 12a. Integration of this hypothetical curve, which by the nature of the extrapolation, excludes a small portion of the measured data in the low pO_2 region, produces the result presented in Figure 12b. The result from this treatment is compared to the experimentally measured oxygen content[40,42] as well as to the value that would be obtained from utilizing the chemical capacitance data from the reducing conditions alone.

Overall, although a sharp change in chemical capacitance at an arbitrary pO_2, as given in the hypothetical curve, is unrealistic, the oxygen content computed using this curve (solid green line) matches the thermogravimetric results quite well, particularly considering that the two experimental data sets reported in the prior literature themselves reflect some disagreement. In contrast, the result that would be obtained from utilizing only the low pO_2 chemical capacitance data (dashed brown curve) shows noticeable disagreement from the

https://doi.org/10.1021/acsami.2c05417
ACS Appl. Mater. Interfaces 2022, 14, 19629−19643

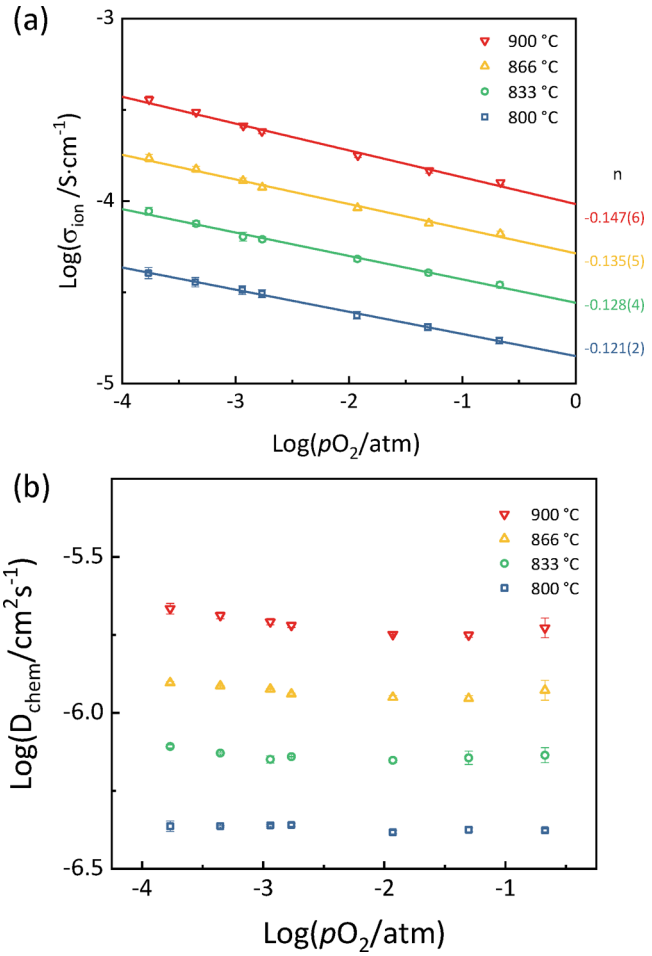

Figure 10. Transport properties of CZO20 under oxidizing conditions deduced from impedance analysis: (a) ionic conductivity; and (b) oxygen chemical diffusivity as functions of oxygen partial pressure, at the temperatures indicated. The number in parentheses following the value of the power law exponent in panel a is the fitting uncertainty in the last digit.

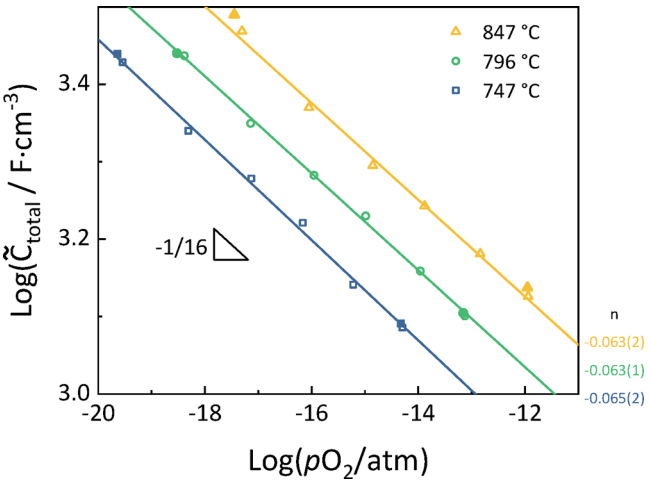

Figure 11. Total capacitance (volume-normalized) of CZO20 under reducing conditions as a function of oxygen partial pressure at the temperatures indicated and deduced from impedance fitting according to the equivalent circuit shown in Figure 1c. Equivalence of the results obtained from the 230 nm thick film (open symbols) and the 460 nm thick film (solid symbols) implies that the total capacitance is dominated by the very large chemical capacitance encountered at under reducing conditions. The number in parentheses following the value of the power law exponent is the fitting uncertainty in the last digit.

thermogravimetric reports, significantly overestimating the oxygen nonstoichiometry even at some of the conditions at which the electrochemical measurements were made (10^{-16} to 10^{-13} atm). This occurs because extrapolation of the low pO_2 chemical capacitance data to high pO_2 would dramatically overestimate the chemical capacitance (at high pO_2) and hence also the oxygen nonstoichiometry. Thus, despite the uncertainty inherent in a large extrapolation across a wide oxygen partial pressure range, the electrochemical measurements provide reliable values of the oxygen nonstoichiometry so long as data close to the limit of $\delta \rightarrow 0$ are included in the measurement campaign and subsequent analysis. While details regarding the ideality of the solution properties remain unresolved, it is apparent from comparison of Figures 6a and 12b that the electrochemical measurement confirms the substantial reduction of Ce that results upon introduction of zirconia in ceria.[40,42] As discussed in the prior studies, the small size of Zr is unsuited to the 8-fold coordination of cations by oxygen in the fluorite structure. The preference of Zr for a lower coordination number drives the generation of oxygen vacancies, which are charge balanced by reduction of Ce to the 3+ oxidation state.

As noted in section 2.1, the formalism employed here is, in principle, applicable also to a material in which the redox activity occurs via incorporation of oxygen into interstitial sites, with electron holes providing the overall charge balance. As in the oxygen vacancy problem explicitly treated in this work, the challenge lies in identifying conditions at which the nonstoichiometry is close to zero, or at least displays a dependence on oxygen partial pressure that can be extrapolated to zero nonstoichiometry. Without prior knowledge of the material properties, precisely establishing the conditions that result in a sufficiently small value of nonstoichiometry is challenging. However, it may be reasonable to conclude that measurements that include a deviation of oxygen stoichiometry, whether δ (vacancies) or β (interstitials), of 10^{-3} will provide the needed data. This nonstoichiometry value can be translated into a value of chemical capacitance by noting $\overline{\varepsilon}_{chem} \approx \frac{F^2}{RTV_m}\delta$ (after eqs 16 and 18), with a similar relationship for β. At a temperature of ~1000 K and with a ceria molar volume of ~ 10 cm^3/mol, the measurement should then include chemical capacitance values at least as small as ~100 F/cm^3. This criterion has been met in the present work.

5. CONCLUSIONS

Using ceria and ceria-zirconia, we have demonstrated a general EIS approach to measure the nonstoichiometry of MIECs with good accuracy. The approach relies on (1) deposition of thin MIEC films on a pure ionic conductor, (2) accurate extraction of the chemical capacitance from the impedance measurement, and (3) recovery of δ from the chemical capacitance using an appropriate mathematical formalism in combination with measurements close to the $\delta \rightarrow 0$ limit. Nonideal solution behavior of undoped ceria under reducing conditions and temperatures between 750 and 900 °C has been confirmed, with a power law exponent relating the chemical capacitance with oxygen partial pressure that varied with pO_2. Using a

https://doi.org/10.1021/acsami.2c05417
ACS Appl. Mater. Interfaces 2022, 14, 19629−19643

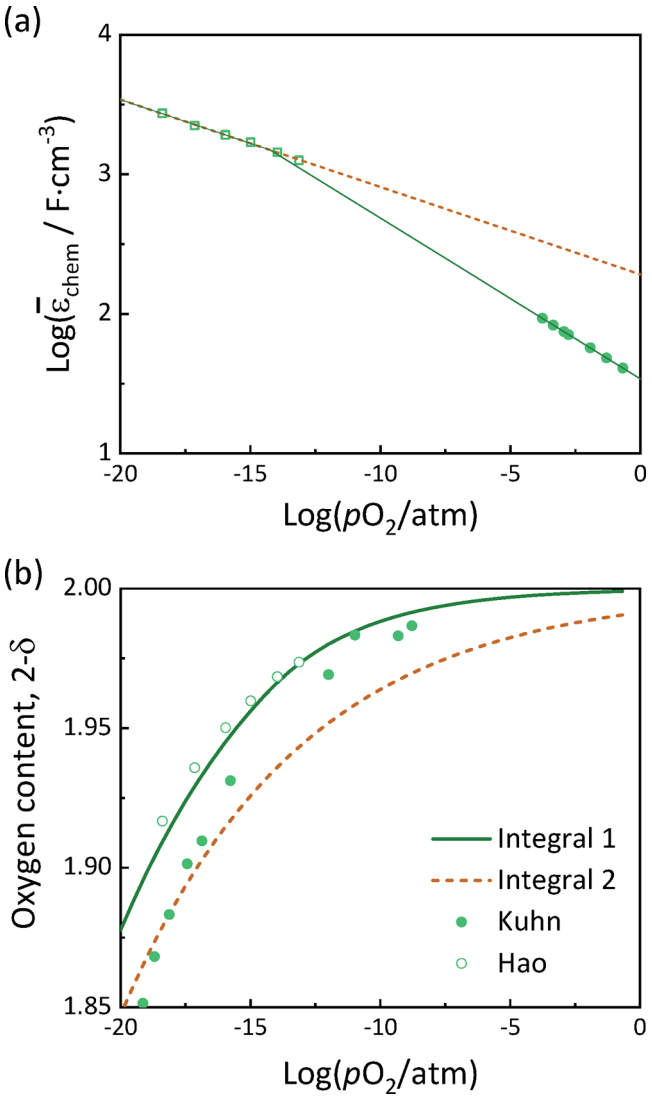

Figure 12. Thermochemical properties of CZO20 across both oxidizing and reducing conditions at 800 ± 3 °C: (a) chemical capacitance; and (b) oxygen content obtained by integration of chemical capacitance measurement under reducing conditions only (brown dashed curve) and by integration of chemical capacitance under both reducing and oxidizing conditions (green solid curve). Shown in panel b are also the thermogravimetric results of Kuhn et al.[40] and of Hao et al.[42]

piecewise numerical integration, and a van't Hoff analysis of the resulting nonstoichiometry data, the standard partial molar enthalpy and standard partial molar entropy of oxygen in ceria at $\delta \approx 6.5 \times 10^{-3}$ were found to be −472 ± 5 kJ/mol-O and −263 ± 5 J/K/mol-O, respectively, falling within the ranges reported in previous studies. In the case of CZO20, the power law exponent in the chemical capacitance was smaller (in magnitude) than the −1/6 value expected for ideal solution behavior though, unlike the case of ceria, independent of pO_2. Under oxidizing conditions, the exponent was ∼−1/8, whereas under reducing conditions it was ∼−1/16. The nonstoichiometry determined from integration of the chemical capacitance values obtained in the oxidizing condition was found to be within about 30% of prior literature results, indicating again ability to measure δ with reasonable accuracy to as low 1×10^{-3}. Using a treatment that imposes the formalism of ideal solution behavior despite the deviation of the power law exponent from −1/6 yielded a standard partial molar enthalpy of oxygen in CZO20 under $pO_2 = 1.7 \times 10^{-4}$ atm of −207 ± 4 kJ/mol-O yields, confirming the remarkably reducibility that Zr imparts on ceria. The nonstoichiometry at low pO_2 was evaluated by integrating C_{chem} from high to low pO_2, where the intermediate pO_2 data were generated by extrapolation from high pO_2. Despite the arbitrary nature of the extrapolation, the nonstoichiometry obtained is also in good agreement with prior literature. The electrochemical measurements also revealed the oxygen ion conductivity in CZO20 at oxidizing conditions, under which the ionic transference number is extremely low and hence ionic conductivity measurements are difficult by other means. The ionic conductivity and chemical capacitance were found to display similar dependences on oxygen partial pressure, implying a chemical diffusion coefficient that is largely independent of pO_2. Such behavior generally results when D_{chem} is dominated by the oxygen vacancy diffusivity ($D_{V_O^{\bullet\bullet}}$) and the vacancy diffusivity is itself independent of oxygen vacancy concentration. The former is expected for ceria under oxidizing conditions, and the latter is expected when the vacancy concentration range examined is small as in the present case.

Beyond the insights into ceria-based materials, it is to be emphasized that the thin film EIS approach is inherently faster than conventional methods requiring bulk samples and furthermore has better sensitivity for detecting small values of nonstoichiometry. The work here expands the applicability of this approach, which has previously been limited to a few model compounds to arbitrary MIEC oxides for which a defect chemical model may not be *a priori* available. Though not exploited here, an additional benefit of the EIS approach is the possibility of using an electrical bias to set the oxygen chemical potential to an arbitrary value, a step that can provide data in the intermediate pO_2 regime[45] and avoid wide interpolations between high and low pO_2 regions accessible through gas mixing. Furthermore, although a discussion of the surface reaction constant is beyond the scope of this work, this parameter is inherently available from the impedance measurement, providing yet another advantage of this approach.

APPENDIX

Equivalent Circuit Descriptions

The impedance of the circuit shown in Figure 1b is given as[26]

$$Z = \frac{R_{ion}Z_D + Z_D Z_A a \coth(a)}{R_{ion} + Z_A Z_D a^2/R_{ion} + (Z_A + Z_D)a \coth(a)} + R_0 \quad \text{(A.1)}$$

where $Z_D = \frac{1}{j\omega C_{eon}^{int}}$, $Z_A = \frac{R_{ion}^{surf}}{1 + R_{ion}^{surf} C_{ion}^{surf}}$, and $a = \sqrt{j\omega R_{ion} C_{chem}}$.

The six fit parameters in this model are C_{chem}, R_{ion}, C_{ion}^{surf}, R_{ion}^{surf}, C_{eon}^{int}, and R_0, where the latter is identical to R_{ion}^{sub}. The term R_{ion}^{surf} is the surface electrochemical reaction resistance. In the limit $C_{eon}^{int} \to 0$, eq A.1 reduces to

$$Z = \frac{R_{ion} + Z_A a \coth(a)}{Z_A a^2/R_{ion} + a \coth(a)} + R_0 \quad \text{(A.2)}$$

from which the desired terms, C_{chem} and R_{ion}, can (still) be determined.

https://doi.org/10.1021/acsami.2c05417
ACS Appl. Mater. Interfaces 2022, 14, 19629−19643

■ ASSOCIATED CONTENT

Supporting Information

The Supporting Information is available free of charge at https://pubs.acs.org/doi/10.1021/acsami.2c05417.

Additional details regarding impedance data and analysis, including extraction of thermodynamic parameters for undoped ceria (PDF)

■ AUTHOR INFORMATION

Corresponding Author

Sossina M. Haile − *Department of Materials Science and Engineering, Department of Applied Physics, and Department of Chemistry, Northwestern University, Evanston, Illinois 60208, United States;* orcid.org/0000-0002-5293-6252; Email: Sossina.haile@northwestern.edu

Authors

Ruiyun Huang − *Department of Materials Science and Engineering, Northwestern University, Evanston, Illinois 60208, United States*

Connor G. Carr − *Department of Materials Science and Engineering, Northwestern University, Evanston, Illinois 60208, United States;* orcid.org/0000-0003-1494-9797

Chirranjeevi Balaji Gopal − *Department of Materials Science, California Institute of Technology, Pasadena, California 91125, United States*

Complete contact information is available at: https://pubs.acs.org/10.1021/acsami.2c05417

Notes

The authors declare no competing financial interest.

■ ACKNOWLEDGMENTS

This work was supported by the US Department of Energy under Office Energy Efficiency and Renewable Energy, Contract No. DE-EE0008089. Additional support was provided by the US National Science Foundation under Award No. DMR-1505103. This work made use of the Pulsed Laser Deposition Shared Facility at the Materials Research Center at Northwestern University supported by the National Science Foundation MRSEC program (DMR-1720139) and the Soft and Hybrid Nanotechnology Experimental (SHyNE) Resource (ECCS-1542205).

■ REFERENCES

(1) Haile, S. M. Fuel cell materials and components. *Acta Mater.* **2003**, *51* (19), 5981−6000.

(2) Jacobson, A. J. Materials for Solid Oxide Fuel Cells. *Chem. Mater.* **2010**, *22* (3), 660−674.

(3) Adler, S. B. Factors Governing Oxygen Reduction in Solid Oxide Fuel Cell Cathodes. *Chem. Rev.* **2004**, *104* (10), 4791−4844.

(4) Trovarelli, A. Catalytic Properties of Ceria and CeO_2-Containing Materials. *Catal. Rev.* **1996**, *38* (4), 439−520.

(5) Chueh, W. C.; Falter, C.; Abbott, M.; Scipio, D.; Furler, P.; Haile, S. M.; Steinfeld, A. High-Flux Solar-Driven Thermochemical Dissociation of CO_2 and H_2O Using Nonstoichiometric Ceria. *Science* **2010**, *330* (6012), 1797−1801.

(6) Abanades, S.; Legal, A.; Cordier, A.; Peraudeau, G.; Flamant, G.; Julbe, A. Investigation of Reactive Cerium-based Oxides for H_2 Production by Thermochemical Two-step Water-splitting. *J. Mater. Sci.* **2010**, *45* (15), 4163−4173.

(7) Scheffe, J. R.; Steinfeld, A. Thermodynamic Analysis of Cerium-Based Oxides for Solar Thermochemical Fuel Production. *Energy Fuels* **2012**, *26* (3), 1928−1936.

(8) Kubicek, M.; Bork, A. H.; Rupp, J. L. M. Perovskite Oxides − a Review on a Versatile Material Class for Solar-to-Fuel Conversion Processes. *Journal of Materials Chemistry A* **2017**, *5* (24), 11983−12000.

(9) Mastronardo, E.; Qian, X.; Coronado, J. M.; Haile, S. M. The Favourable Thermodynamic Properties of Fe-doped $CaMnO_3$ for Thermochemical Heat Storage. *Journal of Materials Chemistry A* **2020**, *8* (17), 8503−8517.

(10) Panlener, R. J.; Blumenthal, R. N.; Garnier, J. E. Thermodynamic Study of Nonstoichiometric Cerium Dioxide. *J. Phys. Chem. Solids* **1975**, *36* (11), 1213−1222.

(11) Patrakeev, M. V.; Leonidov, I. A.; Kozhevnikov, V. L.; Kharton, V. Ion-Electron Transport in Strontium Ferrites: Relationships with Structural Features and Stability. *Solid State Sci.* **2004**, *6* (9), 907−913.

(12) Lai, W.; Haile, S. M. Impedance Spectroscopy as a Tool for Chemical and Electrochemical Analysis of Mixed Conductors: A Case Study of Ceria. *J. Am. Ceram. Soc.* **2005**, *88* (11), 2979−2997.

(13) Maier, J. Chemical Resistance and Chemical Capacitance. *Z.Naturforsch.(B)* **2020**, *75* (1−2), 15−22.

(14) Jamnik, J.; Maier, J. Generalised Equivalent Circuits for Mass and Charge Transport: Chemical Capacitance and its Implications. *Phys. Chem. Chem. Phys.* **2001**, *3* (9), 1668−1678.

(15) Kawada, T.; Suzuki, J.; Sase, M.; Kaimai, A.; Yashiro, K.; Nigara, Y.; Mizusaki, J.; Kawamura, K.; Yugami, H. Determination of Oxygen Vacancy Concentration in a Thin Film of $La_{0.6}Sr_{0.4}CoO_{3-\delta}$ by an Electrochemical Method. *J. Electrochem. Soc.* **2002**, *149* (7), E252−E259.

(16) Chueh, W. C.; Haile, S. M. Electrochemical Studies of Capacitance in Cerium Oxide Thin Films and its Relationship to Anionic and Electronic Defect Densities. *Phys. Chem. Chem. Phys.* **2009**, *11* (37), 8144−8148.

(17) Chen, D.; Bishop, S. R.; Tuller, H. L. Non-stoichiometry in oxide thin films operating under anodic conditions: A chemical capacitance study of the praseodymium-cerium oxide system. *Chem. Mater.* **2014**, *26* (22), 6622−6627.

(18) Kim, G. T.; Wang, S. Y.; Jacobson, A. J.; Yuan, Z.; Chen, C. L. Impedance Studies of Dense Polycrystalline Thin Films of $La_2NiO_{4+\delta}$. *J. Mater. Chem.* **2007**, *17* (13), 1316−1320.

(19) Schmid, A.; Rupp, G. M.; Fleig, J. Voltage and Partial Pressure Dependent Defect Chemistry in (La,Sr)$FeO_{3-\delta}$ Thin Films Investigated by Chemical Capacitance Measurements. *Phys. Chem. Chem. Phys.* **2018**, *20* (17), 12016−12026.

(20) Schmitt, R.; Nenning, A.; Kraynis, O.; Korobko, R.; Frenkel, A. I.; Lubomirsky, I.; Haile, S. M.; Rupp, J. L. M. A Review of Defect Structure and Chemistry in Ceria and its Solid Solutions. *Chem. Soc. Rev.* **2020**, *49* (2), 554−592.

(21) Chiodelli, G.; Flor, G.; Scagliotti, M. Electrical Properties of the ZrO_2-CeO_2 System. *Solid State Ionics* **1996**, *91* (1−2), 109−121.

(22) Bishop, S. R.; Duncan, K. L.; Wachsman, E. D. Defect Equilibria and Chemical Expansion in Non-stoichiometric Undoped and Gadolinium-doped Cerium oxide. *Electrochim. Acta* **2009**, *54* (5), 1436−1443.

(23) Hao, Y.; Yang, C. K.; Haile, S. M. Ceria-Zirconia Solid Solutions ($Ce_{1-x}Zr_xO_{2-\delta}$, $x \leq 0.2$) for Solar Thermochemical Water Splitting: A Thermodynamic Study. *Chem. Mater.* **2014**, *26* (20), 6073−6082.

(24) Chen, D.; Cao, Y. D.; Weng, D.; Tuller, H. L. Defect and Transport Model of Ceria-zirconia Solid Solutions: $Ce_{0.8}Zr_{0.2}O_{2-\delta}$ - an Electrical Conductivity Study. *Chem. Mater.* **2014**, *26* (17), 5143−5150.

(25) Reidy, R. F.; Simkovich, G. Electrical Conductivity and Point Defect behavior in Ceria-Stabilized Zirconia. *Solid State Ionics* **1993**, *62* (1−2), 85−97.

(26) Usiskin, R. E.; Maruyama, S.; Kucharczyk, C. J.; Takeuchi, I.; Haile, S. M. Probing the Reaction Pathway in $(La_{0.8}Sr_{0.2})_{0.95}MnO_{3+\delta}$

Using Libraries of Thin Film Microelectrodes. *Journal of Materials Chemistry A* **2015**, *3* (38), 19330−19345.
(27) Chen, D.; Bishop, S. R.; Tuller, H. L. Non-stoichiometry in Oxide Thin Films: A Chemical Capacitance Study of the Praseodymium-Cerium Oxide System. *Adv. Funct. Mater.* **2013**, *23* (17), 2168−2174.
(28) Brichzin, V.; Fleig, J.; Habermeier, H. U.; Cristiani, G.; Maier, J. The Geometry Dependence of the Polarization Resistance of Sr-doped $LaMnO_3$ Microelectrodes on Yttria-stabilized Zirconia. *Solid State Ionics* **2002**, *152*, 499−507.
(29) Yeh, T. C.; Perry, N. H.; Mason, T. O. Nanograin Composite Model Studies of Nanocrystalline Gadolinia-Doped Ceria. *J. Am. Ceram. Soc.* **2011**, *94* (4), 1073−1078.
(30) Laguna, O. H.; Perez, A.; Centeno, M. A.; Odriozola, J. A. Synergy between Gold and Oxygen Vacancies in Gold Supported on Zr-doped Ceria Catalysts for the CO Oxidation. *Appl. Catal., B* **2015**, *176*, 385−395.
(31) Badwal, S. P. S. Electrical Conductivity of Single Crystal and Polycrystalline Yttria-Stabilized Zirconia. *J. Mater. Sci.* **1984**, *19* (6), 1767−1776.
(32) Yuan, W. Z.; Ma, Q.; Liang, Y. G.; Sun, C. J.; Narayanachari, K.; Bedzyk, M. J.; Takeuchi, I.; Haile, S. M. Unexpected Trends in the Enhanced Ce^{3+} Surface Concentration in Ceria-Zirconia Catalyst Materials. *Journal of Materials Chemistry A* **2020**, *8* (19), 9850−9858.
(33) Chueh, W. C.; McDaniel, A. H.; Grass, M. E.; Hao, Y.; Jabeen, N.; Liu, Z.; Haile, S. M.; McCarty, K. F.; Bluhm, H.; El Gabaly, F. Highly Enhanced Concentration and Stability of Reactive Ce^{3+} on Doped CeO_2 Surface Revealed In Operando. *Chem. Mater.* **2012**, *24* (10), 1876−1882.
(34) Gopal, C. B.; El Gabaly, F.; McDaniel, A. H.; Chueh, W. C. Origin and Tunability of Unusually Large Surface Capacitance in Doped Cerium Oxide Studied by Ambient-Pressure X-Ray Photoelectron Spectroscopy. *Adv. Mater.* **2016**, *28* (23), 4692−4697.
(35) Duncan, K. L.; Wang, Y. L.; Bishop, S. R.; Ebrahimi, F.; Wachsman, E. D. The Role of Point Defects in the Physical Properties of Nonstoichiometric Ceria. *J. Appl. Phys.* **2007**, *101* (4), 6.
(36) Wang, S. R.; Inaba, H.; Tagawa, H.; Dokiya, M.; Hashimoto, T. Nonstoichiometry of $Ce_{0.9}Gd_{0.1}O_{1.95-x}$. *Solid State Ionics* **1998**, *107* (1−2), 73−79.
(37) Takacs, M.; Scheffe, J. R.; Steinfeld, A. Oxygen Nonstoichiometry and Thermodynamic Characterization of Zr Doped Ceria in the 1573−1773 K Temperature Range. *Phys. Chem. Chem. Phys.* **2015**, *17* (12), 7813−7822.
(38) Huggins, R. A. Simple Method to Determine Electronic and Ionic Components of the Conductivity in Mixed Conductors: A Review. *Ionics* **2002**, *8* (3−4), 300−313.
(39) Riess, I. Measurements of Electronic and Ionic Partial Conductivities in mixed Conductors, without the Use of Blocking Electrodes. *Solid State Ionics* **1991**, *44* (3−4), 207−214.
(40) Kuhn, M.; Bishop, S. R.; Rupp, J. L. M.; Tuller, H. L. Structural Characterization and Oxygen Nonstoichiometry of Ceria-zirconia ($Ce_{1-x}Zr_xO_{2-\delta}$) Solid Solutions. *Acta Mater.* **2013**, *61* (11), 4277−4288.
(41) Lee, J. H.; Yoon, S. M.; Kim, B. K.; Lee, H. W.; Song, H. S. Electrical Conductivity and Defect Structure of CeO_2-ZrO_2 Mixed Oxide. *J. Mater. Sci.* **2002**, *37* (6), 1165−1171.
(42) Hao, Y.; Yang, C. K.; Haile, S. M. Ceria-zirconia Solid Solutions ($Ce_{1-x}Zr_xO_{2-\delta}$, $x \leq 0.2$) for Solar Thermochemical Water Splitting: A Thermodynamic Study. *Chem. Mater.* **2014**, *26* (20), 6073−6082.
(43) Boaro, M.; Trovarelli, A.; Hwang, J. H.; Mason, T. O. Electrical and Oxygen Storage/Release Properties of Nanocrystalline Ceria-Zirconia Solid Solutions. *Solid State Ionics* **2002**, *147* (1−2), 85−95.
(44) Chiang, Y.-M. *Physical Ceramics*; J. Wiley: New York, 1997; pp 238−242.
(45) Chen, D.; Tuller, H. L. Voltage-Controlled Nonstoichiometry in Oxide Thin Films: $Pr_{0.1}Ce_{0.9}O_{2-\delta}$ Case Study. *Adv. Funct. Mater.* **2014**, *24* (48), 7638−7644.

https://doi.org/10.1021/acsami.2c05417
ACS Appl. Mater. Interfaces 2022, 14, 19629−19643